(Preprint) AAS 26-693

HUB REACTION TORQUE REDUCTION FOR SPACECRAFT CONTROL USING ROBOTIC ARM-MOUNTED THRUSTERS

William Schwend[*], Alexander Rogers[†], Hanspeter Schaub[‡]

In-space servicing, assembly, and manufacturing (ISAM) missions increasingly rely on robotic arms to perform close-proximity tasks. Recent spacecraft control concepts have proposed using these robotic arms as reconfigurable mounting points for thrusters, allowing the available control wrench to be changed during a mission. However, rapid arm reconfiguration induces reaction torques on the spacecraft hub that must be countered to preserve pointing performance. This paper evaluates two methods for reducing the hub reaction-torque demands associated with rapid reconfiguration of arm-mounted thrusters. The first method uses smooth joint-motion references within a tracking controller, while the second modifies the joint and thruster allocation problem to penalize large joint motions. Both approaches lead to significant reductions in both the typical and maximum prescribed hub torques experienced by the system. The effect of manipulator redundancy on the performance of the joint-motion-aware allocation method is also evaluated by varying the number of joints in each arm. These results show that both the execution of commanded joint motion and the allocation strategy used to select arm configurations strongly influence the actuator burden required to maintain hub pointing during rapid arm reconfiguration for proximity operations.

INTRODUCTION

Future In-space Servicing, Assembly, and Manufacturing (ISAM) missions will require spacecraft to perform increasingly complex on-orbit tasks, including refueling, repair, upgrade, assembly, and debris removal.[1–3] Robotic manipulators are a key enabling technology for many of these close-proximity mission concepts, as illustrated by proposed missions such as OSAM-1[§] and ClearSpace-1[¶]. Although robotic arms expand mission capability, their motion introduces dynamic coupling with the spacecraft hub, complicating guidance, navigation, and control (GNC) design and potentially disturbing attitude pointing during close-proximity maneuvers.[4–6] Prior work in space robotics has addressed this coupling through coordinated arm–spacecraft control strategies and momentum-management techniques.[7–10] However, these approaches typically assume fixed thruster configurations on the spacecraft hub, which can suffer from thrust inefficiencies due to geometric constraints and thrust cancellation.

[*]Ph.D. Student, Ann and H.J. Smead Department of Aerospace Engineering Science, University of Colorado, Boulder, 80303, AIAA Student Member

[†]M.S. Student, Ann and H.J. Smead Department of Aerospace Engineering Science, University of Colorado, Boulder, 80303, AIAA Senior Member

[‡]Distinguished Professor and Department Chair, Schaden Leadership Chair, Ann and H.J. Smead Department of Aerospace Engineering Sciences, University of Colorado, Boulder, 80303, Fellow of AIAA and AAS

[§]`https://www.nasa.gov/centers-and-facilities/goddard/nasas-robotic-osam-1-mission-completes-its-critical-design-review/`

[¶]`https://www.esa.int/ESA_Multimedia/Images/2025/04/ESA_s_ClearSpace-1_prepares_to_deorbit_ESA_s_Proba-1_satellite`

An emerging alternative is to mount thrusters on the robotic arms, allowing the effective thruster geometry to be reconfigured between firings. Concept images for two such spacecraft are shown in Fig. 1. By repositioning thrusters prior to firing, these architectures can reduce thrust cancellation and, in some cases, achieve full 6 degree-of-freedom (DOF) control with as few as two thrusters.[11–17] This reduction in thruster count offers potential mass, volume, and system-complexity savings relative to conventional fixed-thruster designs. However, the same arm motion that improves the attainable control wrench also generates reaction torques on the spacecraft hub which can disturb attitude pointing.

(a) MEV mission concept art*

(b) LEXI mission concept art†

Figure 1: Concept figures of spacecraft with thrusters mounted on robotic arms

Initial investigations of arm-mounted thruster concepts focused primarily on station-keeping and momentum management for geostationary spacecraft,[11–15] where long maneuver time scales permit slow arm reconfiguration and allow conventional attitude-control systems to reject arm-induced disturbances. More recent work has extended arm-mounted thruster concepts to proximity operations, where maneuver timelines are shorter and pointing requirements are more stringent. In this regime, arm-induced attitude motion is more consequential because loss of pointing may correspond to loss of sensor line-of-sight (LOS) to the target. As a result, proximity-operation applications require not only the generation of the desired control wrench, but also careful management of the hub motion induced while reconfiguring the arms. Reference 16 introduces a loop-dynamics formulation for full 6-DOF proximity operations control using arm-mounted thrusters without supplemental momentum-management devices. However, the approach permits transient hub attitude deviations during arm motion and corrects for them during subsequent thruster firings. More recently, Ref. 18 considers an end-effector-mounted thruster system for translational control during proximity operations while regulating the spacecraft attitude, further highlighting the importance of maintaining pointing during arm reconfiguration. References 17 and 19 address this issue by introducing a prescribed hub-torque strategy that enforces zero hub angular acceleration during arm motion within a cascaded 6-DOF relative-motion control architecture.

Although the prescribed hub-torque architecture preserves hub pointing during arm motion by countering the manipulator-induced hub reaction torques generated during arm reconfiguration, its practical implementation depends on the magnitude and duration of the required torque. In the

*https://news.northropgrumman.com/satellites/northrop-grummans-spacelogistics-continues-revolutionary-satellite-life-extension-work-with-sale-of-third-mission-extension-pod

†https://www.astroscale-us.com/en/news/astroscale-israel-completes-construction-of-new-computer-vision-robotics-lab-and-clean-room

baseline implementation of Ref. 17, the robotic arms are commanded using step changes in desired joint angle to rapidly reconfigure the thruster geometry between control updates. While effective for demonstrating the prescribed hub-torque concept, these commands produce large joint accelerations that map directly into short-duration prescribed hub-torque peaks. These transient peaks are important because they may dominate the sizing requirements for the momentum-management system used to apply the prescribed hub torque. Therefore, the relevant design question is not only whether the hub torque required to preserve pointing can be computed, but how the reconfiguration strategy, allocation method, and manipulator architecture affect the actuator burden required to realize it.

This work focuses on smooth methods to achieve the pointing constrained relative motion control with arm mounted thrusters. The goal is to reduce the peak joint torque requirements of prior work by evaluating how two design choices that strongly impact the prescribed torque demands generated during arm reconfiguration: 1) generating smooth joint-reference profiles for use with a joint-motion tracking controller and 2) modifying the joint and thruster allocation problem to penalize unnecessary joint motion. Filtered input shaping of the commanded joint motion was also considered. However, the results are not included in this study as the phase lag and asymptotic behavior was found to be a critical drawback. As part of the second evaluation, the number of joints in each robotic arm is varied to assess how manipulator redundancy affects the performance of the motion-aware allocation method. The novelty of this study lies in applying and evaluating these design choices for the specific problem of rapidly reconfiguring arm-mounted thrusters while preserving hub pointing during proximity operations. In this application, the arms are not repositioned solely to complete a manipulation task; rather, they are repeatedly reconfigured to realize commanded control wrenches between thrusting opportunities, which can require faster motion than typical free-floating manipulation scenarios. This study therefore provides new insight into how the execution of commanded joint motion, the allocation strategy used to select arm configurations, and the available manipulator redundancy influence the actuator burden associated with prescribed hub-torque control.

The remainder of this paper is organized as follows. The problem formulation, system dynamics, and baseline prescribed hub-torque control architecture are first summarized. The numerical simulation setup is then introduced. The prescribed hub-torque reduction studies are subsequently presented, beginning with the effect of joint-reference profiling and followed by the joint-motion-aware allocation method, including its sensitivity to manipulator redundancy. The paper then concludes with a summary of the main findings.

SYSTEM MODELING

The torque-reduction studies in this work are motivated by the representative close-proximity inspection mission shown in Fig. 2. In this scenario, a deputy spacecraft inspects a chief spacecraft while keeping the chief within the field-of-view of an onboard sensor. To provide control authority during the inspection, the deputy uses thrusters mounted on two 4-DOF robotic arms, as shown in Fig. 3. The spacecraft is modeled as a collection of rigid bodies connected by hinged joints, with the hub and arm links shown in gray, the joints shown in blue, and the thrusters shown in orange. By rotating the joints, the deputy repositions the arm-mounted thrusters to generate the control wrench required to regulate the spacecraft center-of-mass motion and hub attitude.

The complex multi-body system dynamics are adopted from Ref. 17 and not repeated here for brevity. The equations of motion use Featherstone's generalized-coordinate multi-body formula-

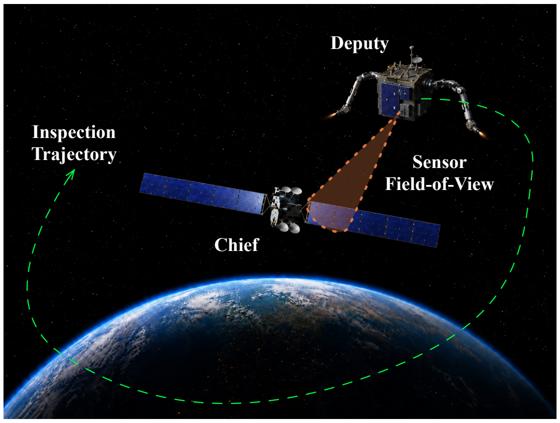

Figure 2: Representative proximity inspection mission

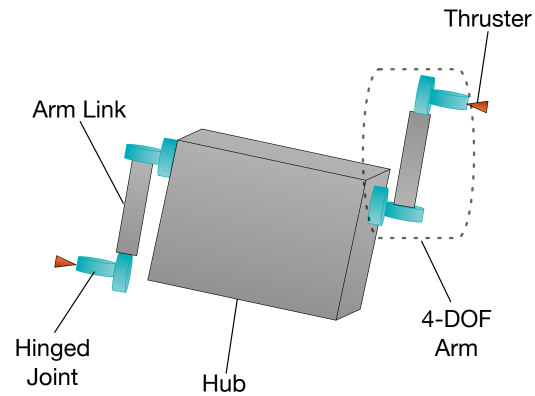

Figure 3: Deputy spacecraft with two 4-DOF thruster arms

tion:[20]

$$\underbrace{\begin{bmatrix} M_{TT} & M_{TR} & M_{T\theta} \\ M_{TR}^T & M_{RR} & M_{R\theta} \\ M_{T\theta}^T & M_{R\theta}^T & M_{\theta\theta} \end{bmatrix}}_{[M(\boldsymbol{q})]} \underbrace{\begin{bmatrix} \ddot{\boldsymbol{r}}_{B/N} \\ \dot{\boldsymbol{\omega}}_{B/N} \\ \ddot{\boldsymbol{\theta}} \end{bmatrix}}_{\ddot{\boldsymbol{q}}} + \underbrace{\begin{bmatrix} \boldsymbol{C}_T \\ \boldsymbol{C}_R \\ \boldsymbol{C}_\theta \end{bmatrix}}_{\boldsymbol{C}(\boldsymbol{q},\dot{\boldsymbol{q}})} = \underbrace{\begin{bmatrix} \boldsymbol{F}_{\text{thr}} \\ \boldsymbol{L}_{\text{thr}} + \boldsymbol{\tau}_{\text{pre}} \\ \boldsymbol{\tau}_{\text{thr}} + \boldsymbol{u}_J \end{bmatrix}}_{\boldsymbol{\tau}} \tag{1}$$

The system coordinates include the position vector from the inertial origin to the spacecraft body-frame origin, $\boldsymbol{r}_{B/N}$; the Modified Rodrigues Parameter (MRP) set describing the orientation of the hub body frame $\mathcal{B}$ relative to the inertial frame $\mathcal{N}$, $\boldsymbol{\sigma}_{B/N}$; the angular velocity of $\mathcal{B}$ relative to $\mathcal{N}$, $\boldsymbol{\omega}_{B/N}$; and the joint angles, $\boldsymbol{\theta}$. The configuration-dependent system mass matrix is denoted by $[M(\boldsymbol{q})]$, while $\boldsymbol{C}(\boldsymbol{q}, \dot{\boldsymbol{q}})$ contains the non-actuator generalized bias forces arising from configuration-dependent effects such as Coriolis, centrifugal, and gravitational effects. Finally, $\boldsymbol{\tau}$ is the vector of actuator-based generalized forces. This vector contains the translational force generated on the spacecraft hub by the thrusters, $\boldsymbol{F}_{\text{thr}}$; the rotational torque generated on the spacecraft hub by the thrusters, $\boldsymbol{L}_{\text{thr}}$; the control torque applied to the hub to counteract the reaction torques generated by arm motion, $\boldsymbol{\tau}_{\text{pre}}$; the torque experienced by the joints during thruster firing, $\boldsymbol{\tau}_{\text{thr}}$; and the joint control torque, $\boldsymbol{u}_J$.

These dynamics can be simulated using a variety of general multi-body solvers, as detailed in Ref. 17. In this work, the open-source physics engine MuJoCo is used through its integration with the astrodynamics simulator Basilisk.[21–23]

OVERVIEW OF CONTROL DESIGN

For close-proximity missions such as the representative inspection scenario shown in Fig. 2, the control objective is to regulate the deputy's relative translation while keeping its sensor boresight directed toward the chief spacecraft. This objective is complicated by the use of arm-mounted thrusters because robotic-arm reconfiguration induces reaction torques on the spacecraft hub. These reaction torques can disturb the hub attitude and potentially violate the pointing constraints imposed by the narrow field-of-view (FOV) of the deputy's sensing instruments.

This work therefore uses the cascaded control architecture developed in Ref. 17 and summarized in Fig. 4. During arm reconfiguration, this architecture applies a prescribed hub torque to enforce $\dot{\boldsymbol{\omega}}_{B/N} = \mathbf{0}$, thereby maintaining pointing performance as the arms move. The architecture is reviewed here to define the baseline control formulation and notation used in the torque-reduction studies that follow.

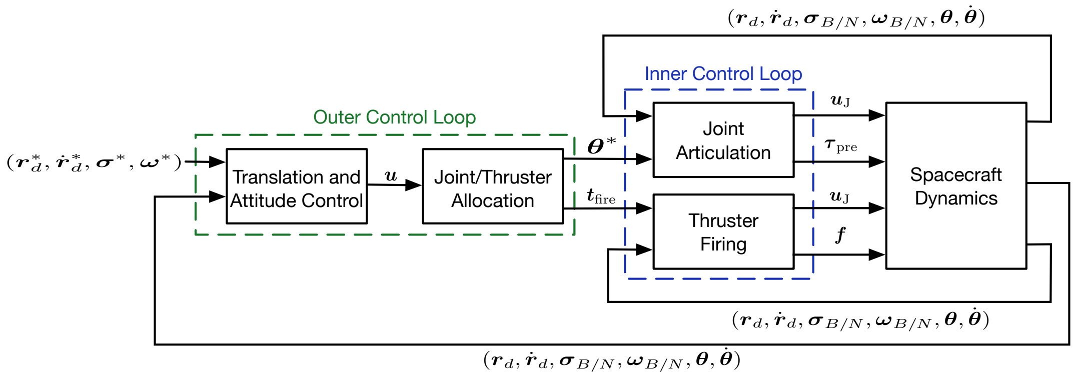

Figure 4: Cascaded control loop design, reproduced from Ref. 17

Outer-Loop Control

The outer control loop computes the desired spacecraft control wrench

$$\boldsymbol{u} = \begin{bmatrix} \boldsymbol{F}_{\text{thr}} \\ \boldsymbol{L}_{\text{thr}} \end{bmatrix}, \tag{2}$$

where $\boldsymbol{F}_{\text{thr}}$ and $\boldsymbol{L}_{\text{thr}}$ are the commanded translational force and rotational torque, respectively. The translational control force is applied at the deputy system center of mass (CoM), whose state is computed from the hub state and the joint-dependent arm geometry as detailed in Ref. 17. Following the Cartesian tracking formulation in Ref. 24, the commanded translational force is

$$\boldsymbol{F}_{\text{thr}} = -(\boldsymbol{F}_d - \boldsymbol{F}_d^*) - [K_T]\Delta\boldsymbol{r} - [P_T]\Delta\dot{\boldsymbol{r}} + \boldsymbol{F}_{\text{thr}}^*, \tag{3}$$

where $\Delta\boldsymbol{r} = \boldsymbol{r}_d - \boldsymbol{r}_d^*$ and $\Delta\dot{\boldsymbol{r}} = \dot{\boldsymbol{r}}_d - \dot{\boldsymbol{r}}_d^*$. Here, $\boldsymbol{F}_d$ and $\boldsymbol{F}_d^*$ are the external non-control forces acting on the current and desired deputy trajectories, $\boldsymbol{F}_{\text{thr}}^*$ is the ideal force required to maintain the desired relative trajectory, and $[K_T]$ and $[P_T]$ are positive-definite gain matrices.

The attitude-control torque is computed using the MRP feedback law

$$\boldsymbol{L}_{\text{thr}} = -K_R\delta\boldsymbol{\sigma} - [P_R]\delta\boldsymbol{\omega} + [I_H]\left(\dot{\boldsymbol{\omega}}^* - [\tilde{\omega}]\boldsymbol{\omega}^*\right) + [\tilde{\omega}][I_H]\boldsymbol{\omega}_{B/N} - \boldsymbol{L}_{\text{ext}}, \tag{4}$$

where the feedback structure follows Ref. 24 and the use of the fixed hub inertia approximation $[I_H]$ follows Ref. 17. The quantities K_R and $[P_R]$ are the attitude feedback gains, $\delta\boldsymbol{\sigma}$ is the MRP attitude tracking error, and $\delta\boldsymbol{\omega} = \boldsymbol{\omega}_{B/N} - \boldsymbol{\omega}^*$.

Joint and Thruster Allocation

The commanded wrench is mapped into a desired joint configuration $\boldsymbol{\theta}^*$ and thruster force magnitudes $\boldsymbol{f}^*$ using the allocation approach of Ref. 14. The allocation problem is

$$\min_{\boldsymbol{\theta}^*,\boldsymbol{f}^*} \left(\boldsymbol{u} - \boldsymbol{u}_{\text{ctl}}(\boldsymbol{\theta}^*, \boldsymbol{f}^*)\right)^T [W_u] \left(\boldsymbol{u} - \boldsymbol{u}_{\text{ctl}}(\boldsymbol{\theta}^*, \boldsymbol{f}^*)\right) + \boldsymbol{W}_f^T \boldsymbol{f}^* \tag{5}$$

subject to

$$\boldsymbol{\theta}_{\min} \leq \boldsymbol{\theta}^* \leq \boldsymbol{\theta}_{\max}, \quad \boldsymbol{0} \leq \boldsymbol{f}^* \leq \boldsymbol{f}_{\max}. \tag{6}$$

Here, $[W_u]$ and $\boldsymbol{W}_f$ penalize control-wrench error and total thrust usage, respectively. The wrench produced by a candidate solution is

$$\boldsymbol{u}_{\text{ctl}}(\boldsymbol{\theta}^*, \boldsymbol{f}^*) = [T(\boldsymbol{\theta}^*)]\boldsymbol{f}^*, \tag{7}$$

where $[T(\boldsymbol{\theta}^*)]$ is the configuration-dependent thruster mapping matrix. The resulting force magnitudes are converted into thruster on-times using a zero-order-hold assumption on the outer-loop command.

Inner-Loop Control

The inner loop executes the allocated command in two phases. During the joint-actuation phase, the thrusters are inactive and the arms are driven to $\boldsymbol{\theta}^*$ while $\boldsymbol{\tau}_{\text{pre}}$ enforces $\dot{\boldsymbol{\omega}}_{B/N} = \boldsymbol{0}$. Under these assumptions, the reduced joint-actuation dynamics are

$$[\overline{M}]\ddot{\boldsymbol{\theta}} = \boldsymbol{u}_J - \overline{\boldsymbol{C}}, \tag{8a}$$

$$M_{TT}\ddot{\boldsymbol{r}}_{B/N} = -\boldsymbol{C}_T - M_{T\theta}\ddot{\boldsymbol{\theta}}, \tag{8b}$$

where

$$[\overline{M}] = M_{\theta\theta} - M_{T\theta}^T M_{TT}^{-1} M_{T\theta}, \;\; \overline{\boldsymbol{C}} = \boldsymbol{C}_\theta - M_{T\theta}^T M_{TT}^{-1} \boldsymbol{C}_T. \tag{9}$$

The baseline regulation controller is

$$\boldsymbol{u}_J = [\overline{M}] \left(-[K_\theta]\delta\boldsymbol{\theta} - [P_\theta]\dot{\boldsymbol{\theta}}\right) + \overline{\boldsymbol{C}}, \tag{10}$$

where $\delta\boldsymbol{\theta} = \boldsymbol{\theta} - \boldsymbol{\theta}^*$ and $[K_\theta]$ and $[P_\theta]$ are positive-definite gain matrices. The full derivation and stability proof are provided in Ref. 17.

The prescribed hub torque required to enforce the zero hub angular acceleration condition is

$$\boldsymbol{\tau}_{\text{pre}} = M_{TR}^T \ddot{\boldsymbol{r}}_{B/N} + M_{R\theta}\ddot{\boldsymbol{\theta}} + \boldsymbol{C}_R. \tag{11}$$

During the thruster-firing phase, $\boldsymbol{\tau}_{\text{pre}} = \boldsymbol{0}$ and the thrusters produce the commanded wrench. The joint motors maintain the commanded joint configuration by enforcing $\ddot{\boldsymbol{\theta}} = \boldsymbol{0}$, which gives

$$\boldsymbol{u}_J = M_{T\theta}^T \ddot{\boldsymbol{r}}_{B/N} + M_{R\theta}^T \dot{\boldsymbol{\omega}}_{B/N} + \boldsymbol{C}_\theta - \boldsymbol{\tau}_{\text{thr}}, \tag{12}$$

with

$$\boldsymbol{\tau}_{\text{thr}} = [J]^T \boldsymbol{F}, \tag{13}$$

where $[J]$ maps the stacked thruster force vector $\boldsymbol{F}$ to the corresponding torques at the joints.

NUMERICAL SIMULATION SETUP

The numerical studies in this work use the proximity-operations simulation scenario introduced in Ref. 17 as a fixed baseline for evaluating the proposed prescribed hub-torque reduction methods. Reusing this scenario allows changes in the prescribed hub-torque demand to be attributed to the selected reduction method rather than to changes in the spacecraft geometry, actuator configuration, controller gains, or mission trajectory.

The deputy's desired relative-motion trajectory is shown in Fig. 5. Throughout this trajectory, the attitude-control objective is to keep the deputy's $\hat{b}_1$ axis pointed at the chief spacecraft, providing a representative line-of-sight-constrained inspection scenario. The deputy spacecraft consists of a rectangular-prism hub with two identical 4-DOF arms mounted on the $\pm\hat{b}_1$ faces, as summarized in Table 1. The local spin-axis definitions for each arm joint are listed in Table 2, and each joint is equipped with a motor capable of producing 2.5 Nm of torque. A single thruster is mounted at the end of each arm and produces 0.25 N of thrust along its local $[-1, 0, 0]^T$ direction.

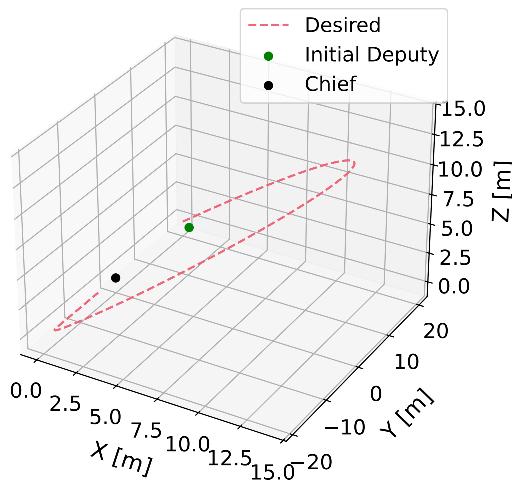

Figure 5: Desired relative motion trajectory

Table 1: Spacecraft mass and inertia properties

Body	**Mass** [kg]	**Inertia** [kg·m^2]
Hub	980	$\begin{bmatrix} 243.929 & 0 & 0 \\ 0 & 292.667 & 0 \\ 0 & 0 & 359.007 \end{bmatrix}$
Joints 1,2 + Boom	8	$\begin{bmatrix} 0.04 & 0 & 0 \\ 0 & 0.687 & 0 \\ 0 & 0 & 0.687 \end{bmatrix}$
Joints 3,4 + Thruster	2	$\begin{bmatrix} 0.0025 & 0 & 0 \\ 0 & 0.021 & 0 \\ 0 & 0 & 0.021 \end{bmatrix}$

Table 2: Arm joint spin-axis definitions

Joint 1	Joint 2	Joint 3	Joint 4
$[1,0,0]^T$	$[0,1,0]^T$	$[0,0,1]^T$	$[0,1,0]^T$

The spacecraft dynamics are simulated using Basilisk's MuJoCo interface in a gravity-free environment with no external forces or torques. This environment isolates the manipulator-induced hub-torque demand, allowing changes in the prescribed hub torque to be attributed to the commanded arm motion rather than to external disturbances. The outer-loop controller is updated at 0.1 Hz, while the multi-body dynamics and inner-loop controller are updated at 100 Hz. The fixed controller gains used for all numerical studies are listed in Table 3, and the baseline initial conditions are listed in Table 4. The joint and thruster allocation problem is solved using multi-start sequential least-squares programming (SLSQP), with the allocation weights $[W_u] = [I_{6\times 6}]$ and $\boldsymbol{W}_f = \mathbf{10^{-4}}$, joint bounds $\boldsymbol{\theta} \in [-\pi, \pi]$, and individual thrust bounds of $0 \leq f_i \leq 0.25$ N.

Table 3: Controller gains

$[\boldsymbol{K_T}]$ [N/m]	$[\boldsymbol{P_T}]$ [N·s/m]	$\boldsymbol{K_R}$ [N·m]	$[\boldsymbol{P_R}]$ [N·m·s]	$[\boldsymbol{K_\theta}]$ [N·m/rad]	$[\boldsymbol{P_\theta}]$ [N·m·s/rad]
$0.02 \times [I_{3\times 3}]$	$50 \times [I_{3\times 3}]$	1.75	$15.0 \times [I_{3\times 3}]$	$22 \times [I_{8\times 8}]$	$14 \times [I_{8\times 8}]$

Table 4: Simulation initial conditions

Parameter	Value
$\boldsymbol{r}_{B/N}(0)$	$[0.5, 19.65, -0.25]^T$ [m]
$\dot{\boldsymbol{r}}_{B/N}(0)$	$[2.5 \times 10^{-3}, -4.0 \times 10^{-4}, 1.75 \times 10^{-3}]^T$ [m/s]
$\boldsymbol{\sigma}_{B/N}(0)$	$[0.16, 0.05, -0.54]^T$
$\boldsymbol{\omega}_{B/N}(0)$	$[1.0 \times 10^{-3}, -2.5 \times 10^{-4}, -9.5 \times 10^{-4}]^T$ [rad/s]
$\boldsymbol{\theta}(0)$	$\mathbf{0}$
$\dot{\boldsymbol{\theta}}(0)$	$\mathbf{0}$

OPTION 1: JOINT-REFERENCE MOTION PROFILING

The numerical simulation setup defined in the previous section provides the baseline case used to evaluate each prescribed hub-torque reduction method. The first modification considered is to replace the step changes in joint reference commanded at each outer-loop control update with finite-duration joint-motion profiles. In the baseline implementation, each new joint configuration is supplied directly to the joint controller as a step command. Because the joint controller is formulated as a regulator, it attempts to remove the resulting tracking error as quickly as permitted by the actuator limits and control gains, producing large initial joint accelerations and elevated transient joint rates. These rapid joint motions generate impulsive reaction torques on the spacecraft hub, consistent with the short-duration peaks observed in the prescribed torque histories.[17] Replacing the step commands with finite-duration profiles reduces the abruptness of the commanded joint motion and can therefore reduce the peak prescribed hub torque required to maintain $\dot{\boldsymbol{\omega}}_{B/N} = \mathbf{0}$ during arm articulation. This section first extends the baseline joint regulator to a tracking controller and then defines the joint-space motion profiles evaluated in the numerical studies.

Joint Tracking Control

Because the motion-profiled references specify time-varying joint angles, rates, and accelerations, the joint regulation controller detailed in the *Inner-Loop Control* section is extended to a tracking controller. This modification allows the commanded trajectory to be followed without treating each intermediate reference as a new step input. The joint tracking errors are defined as

$$\delta\boldsymbol{\theta} = \boldsymbol{\theta} - \boldsymbol{\theta}^*, \;\; \delta\dot{\boldsymbol{\theta}} = \dot{\boldsymbol{\theta}} - \dot{\boldsymbol{\theta}}^*, \tag{14}$$

with the control objective

$$\delta\boldsymbol{\theta} \to 0, \;\; \delta\dot{\boldsymbol{\theta}} \to 0. \tag{15}$$

Here, $\dot{\boldsymbol{\theta}}^*$ denotes the desired joint rates.

Selecting the candidate Lyapunov function

$$V(\delta\boldsymbol{\theta}, \delta\dot{\boldsymbol{\theta}}) = \frac{1}{2}\delta\dot{\boldsymbol{\theta}}^T\delta\dot{\boldsymbol{\theta}} + \frac{1}{2}\delta\boldsymbol{\theta}^T[K_\theta]\delta\boldsymbol{\theta} \tag{16}$$

and taking the derivative yields

$$\dot{V}(\delta\boldsymbol{\theta}, \delta\dot{\boldsymbol{\theta}}) = \delta\dot{\boldsymbol{\theta}}^T\left(\delta\ddot{\boldsymbol{\theta}} + [K_\theta]\delta\boldsymbol{\theta}\right) \tag{17}$$

where

$$\delta\ddot{\boldsymbol{\theta}} = \ddot{\boldsymbol{\theta}} - \ddot{\boldsymbol{\theta}}^* \tag{18}$$

and $\ddot{\boldsymbol{\theta}}^*$ denotes the desired joint accelerations.

To make $\dot{V}$ negative semi-definite, the desired closed-loop error dynamics are selected such that $\dot{V} = -\delta\dot{\boldsymbol{\theta}}^T[P_\theta]\delta\dot{\boldsymbol{\theta}}$. Substituting the expression for $\ddot{\boldsymbol{\theta}}$ from Eq. (8a) gives

$$\delta\dot{\boldsymbol{\theta}}^T\left[[\overline{M}]^{-1}(\boldsymbol{u}_J - \overline{\boldsymbol{C}}) - \ddot{\boldsymbol{\theta}}^* + [P_\theta]\delta\dot{\boldsymbol{\theta}} + [K_\theta]\delta\boldsymbol{\theta}\right] = 0 \tag{19}$$

The control is then found by setting the term inside the brackets to zero yielding

$$\boldsymbol{u}_J = [\overline{M}](\ddot{\boldsymbol{\theta}}^* - [K_\theta]\delta\boldsymbol{\theta} - [P_\theta]\delta\dot{\boldsymbol{\theta}}) + \overline{\boldsymbol{C}} \tag{20}$$

Because V is positive-definite and radially unbounded, and $\dot{V}$ is negative semi-definite, this control law is globally stabilizing. Following the methodology presented by Mukherjee and Chen[25] and shown in Ref. 17, the tracking control law is also found to be asymptotically stabilizing. The corresponding prescribed hub torque is then found using Eq. (11).

Profile Definitions

With the joint tracking controller established, the remaining step is to define the finite-duration reference trajectories supplied to the controller. Three standard reference-shaping methods are considered to evaluate how increasing smoothness in the commanded joint motion affects the prescribed hub-torque demand: a linear profile, a cubic polynomial profile, and a quintic polynomial profile.

These profiles impose different levels of smoothness on the commanded motion. The linear profile removes the position step but introduces velocity discontinuities at the profile endpoints. The cubic profile enforces position and velocity boundary conditions, while the quintic profile additionally enforces acceleration boundary conditions. This progression allows the effect of increasingly restrictive endpoint continuity constraints on the prescribed hub-torque demand to be isolated. For each profile type, the duration T is varied to evaluate the trade between slower joint reconfiguration and reduced prescribed hub-torque demand.

Each method maps the current joint state and final desired joint configuration into a reference consisting of desired joint angles, rates, and accelerations supplied to the tracking controller. The three profiles are defined below for a single joint. In implementation, the same construction is applied independently to each component of $\boldsymbol{\theta}$, allowing the motion profile to be defined separately for each joint.

The three chosen profiles are formulated as point-to-point joint-space trajectories.[26] For each profile, the elapsed time since the start of the profile is denoted by s and the desired joint displacement is

$$\Delta\theta = \theta_f^* - \theta_0, \tag{21}$$

where θ_0 is the joint angle at the start of the profile and θ_f^* is the desired final joint angle. For $s \geq T$, each profile is held fixed at $\theta^* = \theta_f^*$ with $\dot{\theta}^* = 0$ and $\ddot{\theta}^* = 0$.

The simplest point-to-point trajectory is a linear profile, which uses constant-velocity motion to move the joint from θ_0 to θ_f^* over T. The resulting reference is

$$\theta^* = \theta_0 + \frac{s}{T}\Delta\theta, \tag{22a}$$

$$\dot{\theta}^* = \frac{\Delta\theta}{T}, \tag{22b}$$

$$\ddot{\theta}^* = 0. \tag{22c}$$

This profile removes the position step present in the baseline regulation controller, but it introduces discontinuities in the reference velocity at the start and end of the profile.

To increase smoothness, the cubic profile constrains both the joint angle and joint rate at the beginning and end of the maneuver. The boundary conditions are selected as

$$\theta^*(0) = \theta_0, \;\; \dot{\theta}^*(0) = \dot{\theta}_0, \;\; \theta^*(T) = \theta_f^*, \;\; \dot{\theta}^*(T) = 0, \tag{23}$$

where $\dot{\theta}_0$ is the joint rate at the start of the profile. The resulting cubic reference trajectory is

$$\theta^* = a_0 + a_1 s + a_2 s^2 + a_3 s^3, \tag{24a}$$

$$\dot{\theta}^* = a_1 + 2a_2 s + 3a_3 s^2, \tag{24b}$$

$$\ddot{\theta}^* = 2a_2 + 6a_3 s, \tag{24c}$$

with coefficients

$$\begin{gathered} a_0 = \theta_0, \quad a_1 = \dot{\theta}_0, \\ a_2 = \frac{3\Delta\theta}{T^2} - \frac{2\dot{\theta}_0}{T}, \quad a_3 = -\frac{2\Delta\theta}{T^3} + \frac{\dot{\theta}_0}{T^2}. \end{gathered} \tag{25}$$

Finally, the quintic profile further increases smoothness by adding acceleration boundary conditions to those in Eq. (23),

$$\ddot{\theta}^*(0) = 0, \quad \ddot{\theta}^*(T) = 0. \tag{26}$$

The reference trajectory is expanded to a fifth-order polynomial,

$$\theta^* = b_0 + b_1 s + b_2 s^2 + b_3 s^3 + b_4 s^4 + b_5 s^5, \tag{27a}$$

$$\dot{\theta}^* = b_1 + 2b_2 s + 3b_3 s^2 + 4b_4 s^3 + 5b_5 s^4, \tag{27b}$$

$$\ddot{\theta}^* = 2b_2 + 6b_3 s + 12b_4 s^2 + 20b_5 s^3, \tag{27c}$$

where the coefficients are

$$\begin{gathered} b_0 = \theta_0, \quad b_1 = \dot{\theta}_0, \quad b_2 = 0, \\ b_3 = \frac{10\Delta\theta - 6\dot{\theta}_0 T}{T^3}, \quad b_4 = \frac{-15\Delta\theta + 8\dot{\theta}_0 T}{T^4}, \quad b_5 = \frac{6\Delta\theta - 3\dot{\theta}_0 T}{T^5}. \end{gathered} \tag{28}$$

Motion-Profile Results

To evaluate the effectiveness of motion profiling for prescribed hub-torque reduction, each of the three profiles is simulated over profile durations ranging from 4 s to 9.5 s. The linear-profile results are restricted to durations no longer than 8.5 s, as discussed below. The step-reference-command case is included as a baseline and is denoted by a profile duration of 0 s. Figure 6 shows that introducing a finite-duration profile substantially reduces the prescribed hub-torque demand relative to the step-reference-command baseline. For the $\hat{b}_3$ component, the median prescribed torque remains small for all profiled cases, while both the interquartile range (IQR) and middle 90% interval generally decrease as the profile duration is increased, as shown in Fig. 6a. Across the profile types considered, the longest profile durations reduce the IQR and middle 90% interval by approximately 80% relative to the step-reference-command case. For clarity, Fig. 6a shows only the distribution summary of the $\hat{b}_3$ torque component. The corresponding $\hat{b}_1$ and $\hat{b}_2$ components exhibit the same qualitative behavior: introducing any finite-duration profile greatly reduces the prescribed torque demand, after which the values remain small for the durations considered.

The same general reduction trend is observed in the maximum prescribed torques shown in Fig. 6b. At the longest duration considered, the maximum torque components are reduced by approximately 85%–98% for most axes and profile types. The primary exception is the linear-profile $\hat{b}_1$ component, which shows little reduction in maximum torque. However, this component is already much smaller than the dominant $\hat{b}_2$ and $\hat{b}_3$ components in the step-reference-command case, so this lack of reduction does not strongly affect the overall prescribed-torque requirement.

The torque reductions must be interpreted together with the joint-settling behavior shown in Fig. 7. The joint-settling time is defined as the time required for all joints to satisfy $|\theta_i^* - \theta_i| < 10^{-3}$ rad and $|\dot{\theta}_i^* - \dot{\theta}_i| < 10^{-3}$ rad/s. If any joint fails to satisfy these conditions within the outer-loop control period, the corresponding control window is classified as unsettled. The linear-profile results are restricted to profile durations no longer than 8.5 s because the nonzero endpoint velocity causes the median joint-settling time to approach the outer-loop control window for longer profiles, as shown in Fig. 7a. This reduced settling margin also increases the fraction of unsettled control windows, as shown in Fig. 7b. In contrast, the cubic and quintic profiles enforce zero endpoint velocity, and their median settling times remain approximately equal to the commanded profile duration. As a result,

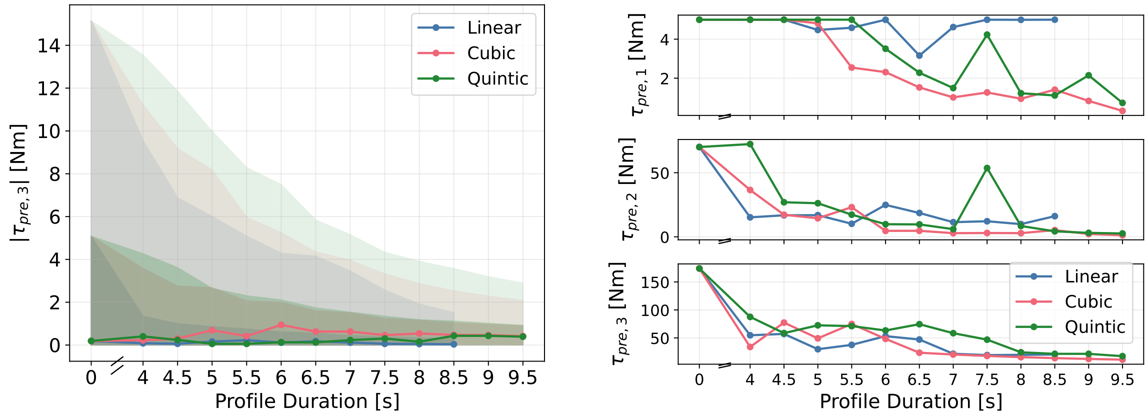

(a) Median, IQR, and middle 90% prescribed hub torques for $\hat{b}_3$ axis

(b) Maximum prescribed hub torques

Figure 6: Change in prescribed hub torque by profile duration

increasing the cubic or quintic profile duration does not produce the same growth in unsettled windows observed for the linear profile. Instead, sufficiently long cubic and quintic profile durations eliminate missed settling windows altogether.

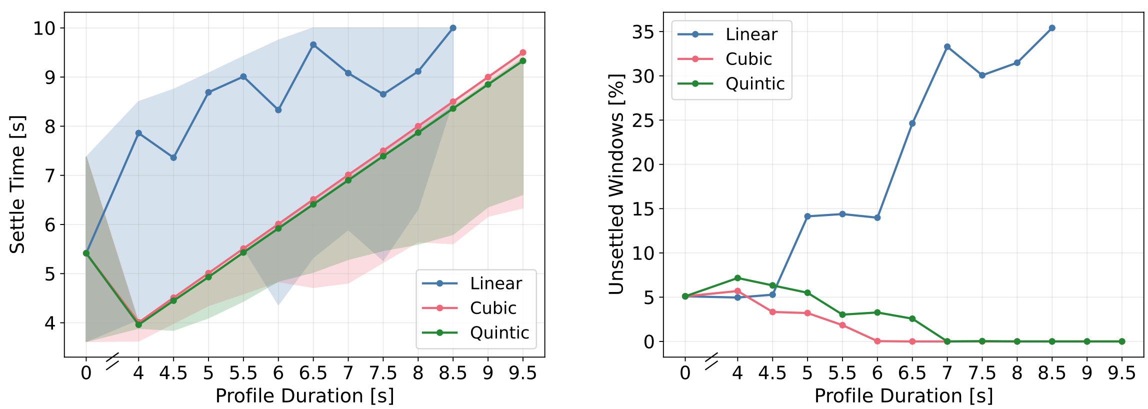

(a) Median and IQR joint settling times

(b) Control windows where joints do not settle

Figure 7: Joint settling performance by profile duration

The effect of motion profiling on closed-loop performance is shown in Fig. 8. Introducing a finite-duration profile reduces the pointing error over the final half of the simulation for all three profile types. The pointing-error improvement is largest when moving from the step-reference-command case to the shortest finite-duration profiles. Further increases in profile duration provide comparatively smaller pointing-error improvements, indicating that most of the pointing benefit is obtained by replacing the instantaneous joint command with a finite-duration trajectory. This improvement is consistent with the reduction in prescribed hub-torque demand: lower prescribed torques reduce the effect of the zero-order hold in the discrete control implementation, improving reaction-torque cancellation and reducing hub angular acceleration during arm motion.

The position-error behavior shows the opposite trend. As the profile duration increases, the position error generally increases, particularly for the longer-duration profiles. This degradation is most pronounced for the linear profile, which also exhibits the poorest joint-settling behavior. For the cubic and quintic profiles, the position error increases more gradually, but still tends to grow at longer profile durations. This trend is consistent with improved pointing performance reducing the attitude-control contribution to the requested control wrench. As the requested wrench decreases, more commanded thruster on-times fall below the minimum on-time of 0.01 s and are rounded to zero. The resulting loss of realized thruster firings reduces translational control authority, causing the position error to increase.

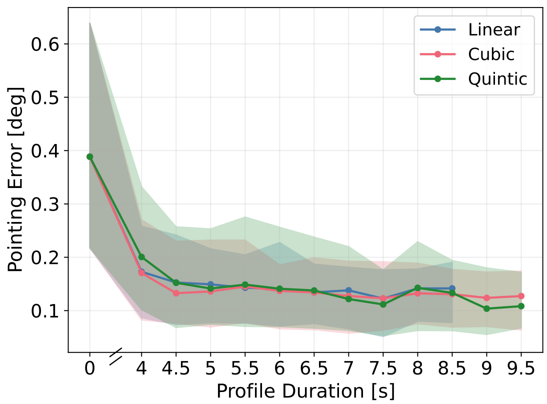

(a) Median and IQR pointing error

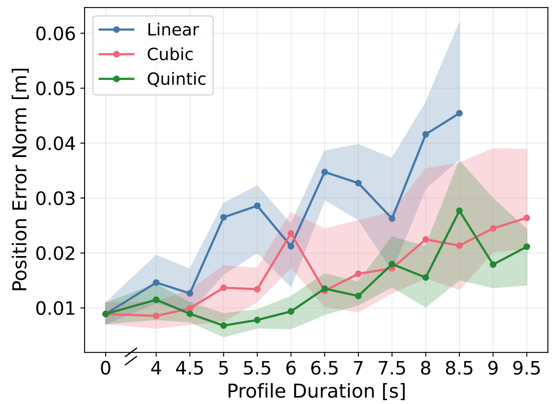

(b) Median and IQR position error

Figure 8: Performance error over final half of simulation by profile duration

This trade is also reflected in the commanded thruster impulse shown in Fig. 9. Introducing a finite-duration profile reduces the commanded impulse relative to the step-reference-command case for all three profile types. For the cubic and quintic profiles, the commanded impulse remains well below the baseline across the durations considered and generally decreases as the profile duration is increased. This reduction is consistent with the improved pointing performance discussed previously, but it also contributes to the growth in position-error when the corresponding commanded on-times fall below the minimum allowable value and are rounded to zero. The linear profile exhibits a different trend. Although it initially reduces the commanded impulse substantially, longer profile durations lead to degraded joint-settling behavior, which alters the subsequent thrusting response and causes the commanded impulse to increase sharply, eventually exceeding the step-reference-command case. Taken together, the poor joint-settling behavior, increased commanded impulse, and worst translational control performance indicate that the linear profile is less suitable for the fixed-window implementation, despite reducing the prescribed hub-torque demand.

Overall, these results show that finite-duration joint profiles substantially reduce the prescribed hub-torque demand while improving pointing performance. However, the profile duration cannot be increased arbitrarily. Longer cubic and quintic profiles provide reliable settling and continued prescribed-torque reduction, but they also reduce the requested control effort and can increase the number of commanded firings that fall below the minimum on-time constraint, reducing realized translational control authority. The linear profile provides prescribed-torque reduction at shorter durations, but its nonzero endpoint velocity makes it poorly suited to the fixed outer-loop control

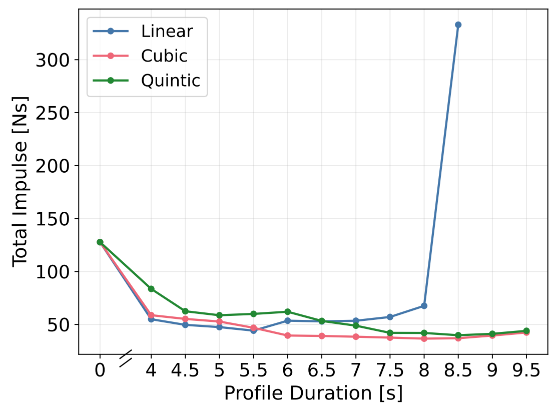

Figure 9: Commanded thruster impulse by profile duration

window as the duration is increased. The profile duration should therefore be selected to balance prescribed-torque reduction, joint-settling reliability, commanded impulse, and position and attitude control performance.

OPTION 2: JOINT-MOTION-AWARE ALLOCATION

The motion-profile results in the previous section reduce prescribed hub-torque demand by changing how a selected joint reconfiguration is executed. However, the prescribed hub-torque demand also depends on which joint reconfiguration is selected by the allocation problem. The two-arm, 4-DOF-per-arm thruster system described in the *Numerical Simulation Setup* section provides configuration redundancy, allowing multiple joint configurations to generate comparable control wrenches. The baseline allocation problem selects among these configurations by balancing wrench-tracking accuracy and thruster effort, without directly considering the size of the required joint reconfiguration. As a result, the allocator may select configurations that require relatively large joint motions between consecutive outer-loop updates, even when smaller joint changes could produce a comparable commanded wrench.

This observation motivates a second torque-reduction approach in which the allocation problem is modified to discourage large joint reconfigurations when comparable wrench-tracking performance can be maintained. Figure 10 compares the average commanded joint-angle changes in the baseline simulation for the control windows associated with the largest 10% of prescribed hub-torque magnitudes about $\hat{b}_3$ and those associated with the remaining 90%. The largest prescribed-torque cases correspond to larger commanded joint changes across all eight joints. For clarity, the corresponding results for the $\hat{b}_1$ and $\hat{b}_2$ axes are omitted, but they exhibit the same qualitative trend. Because larger joint reconfigurations generally require larger joint accelerations and greater internal momentum exchange during finite-duration motion, reducing the commanded joint displacement provides a direct mechanism for reducing transient prescribed hub-torque demand.

Motion-Penalized Allocation Formulation

To encourage smaller joint reconfigurations, the optimization problem in Eq. (5) is augmented with a penalty on the deviation between the current joint configuration and the newly commanded

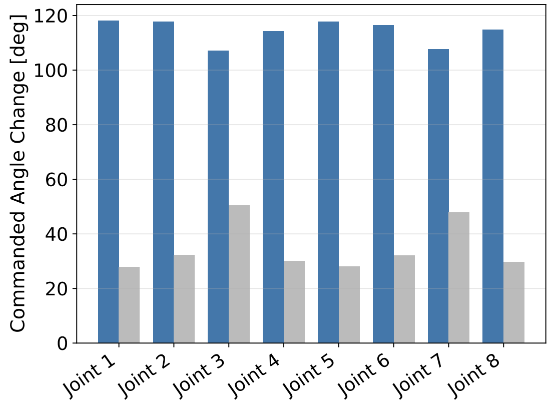

Figure 10: Average commanded joint-angle change associated with the largest 10% (blue) and remaining 90% (gray) of baseline prescribed hub-torque magnitudes about the $\hat{\boldsymbol{b}}_3$ axis

joint configuration:

$$\min_{\boldsymbol{\theta}^*,\boldsymbol{f}^*} \left(\boldsymbol{u} - \boldsymbol{u}_{\text{ctl}}(\boldsymbol{\theta}^*, \boldsymbol{f}^*)\right)^T [W_u] \left(\boldsymbol{u} - \boldsymbol{u}_{\text{ctl}}(\boldsymbol{\theta}^*, \boldsymbol{f}^*)\right) + (\boldsymbol{\theta}^* - \boldsymbol{\theta})^T [W_\theta](\boldsymbol{\theta}^* - \boldsymbol{\theta}) + \boldsymbol{W}_f^T \boldsymbol{f}^* \tag{29}$$

Here, $[W_\theta]$ weights the cost of moving away from the current joint configuration. This term biases the optimizer toward nearby configurations when multiple arm poses can produce similar control wrenches. The added penalty therefore trades some thruster-effort optimality and control-wrench optimality for reduced joint motion.

The remainder of the allocation algorithm is unchanged from the baseline formulation. The same wrench mapping, joint and thruster constraints, and force-to-thruster-on-time conversion are used. Therefore, any changes in prescribed hub-torque demand can be attributed to the addition of the joint-motion penalty rather than to changes in the controller, actuator model, or simulation scenario.

Joint-Motion-Aware Allocation Results

The effect of adding the joint-motion penalty is evaluated by varying the scalar weight W_θ from 0 to 10^{-3}, with $[W_\theta] = W_\theta[I_{8\times8}]$. The case $W_\theta = 0$ corresponds to the baseline allocation problem, in which joint motion is not penalized. Changes with increasing W_θ therefore indicate how biasing the optimizer toward nearby joint configurations affects the prescribed hub-torque demand, closed-loop performance, thruster usage, and joint-settling behavior.

Figure 11 shows that adding the joint-motion penalty reduces both the distribution and maximum values of the prescribed hub torque required to maintain $\dot{\boldsymbol{\omega}}_{B/N} = \boldsymbol{0}$ during arm reconfiguration. The effect is most apparent in the maximum prescribed hub torques, which decrease substantially for the dominant $\hat{b}_2$ and $\hat{b}_3$ components as W_θ is increased. The largest reduction occurs about the $\hat{b}_3$ axis, which is also the axis with the largest prescribed hub-torque requirement in the baseline case. This behavior is consistent with the motivation for the modified allocation problem: when the optimizer is discouraged from selecting configurations that require large joint changes, the resulting arm motion generally produces smaller transient reaction-torque demands on the hub.

The closed-loop performance over the final half of the simulation is shown in Fig. 12. For small and moderate values of W_θ, the pointing and position errors generally decrease relative to the baseline case, with the best overall performance occurring near $W_\theta = 10^{-5}$. At this value, the joint-

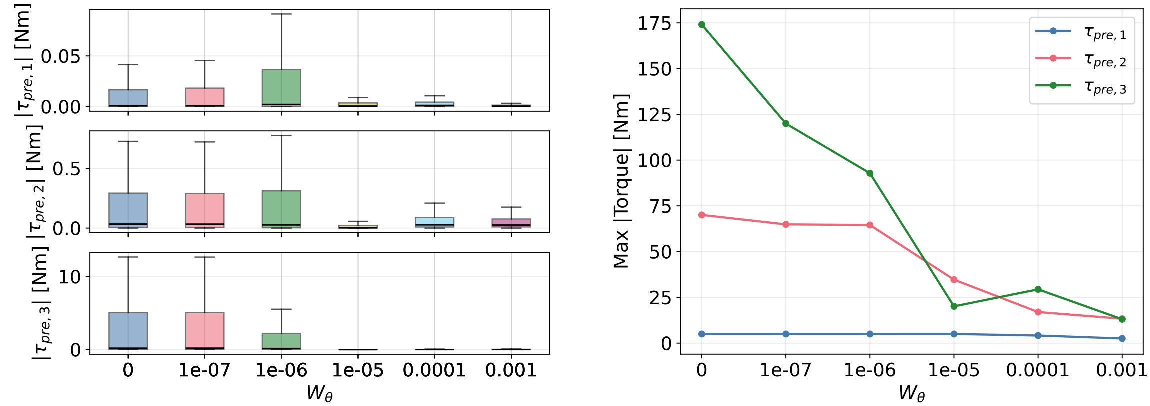

(a) Prescribed hub torque distributions with outliers removed

(b) Maximum prescribed hub torques

Figure 11: Change in prescribed hub torque by joint motion penalty

motion penalty is large enough to reduce unnecessary arm reconfiguration without dominating the wrench-tracking objective. In these cases, the allocation problem increasingly favors small joint changes even when a larger reconfiguration would provide a more effective way to generate the commanded wrench.

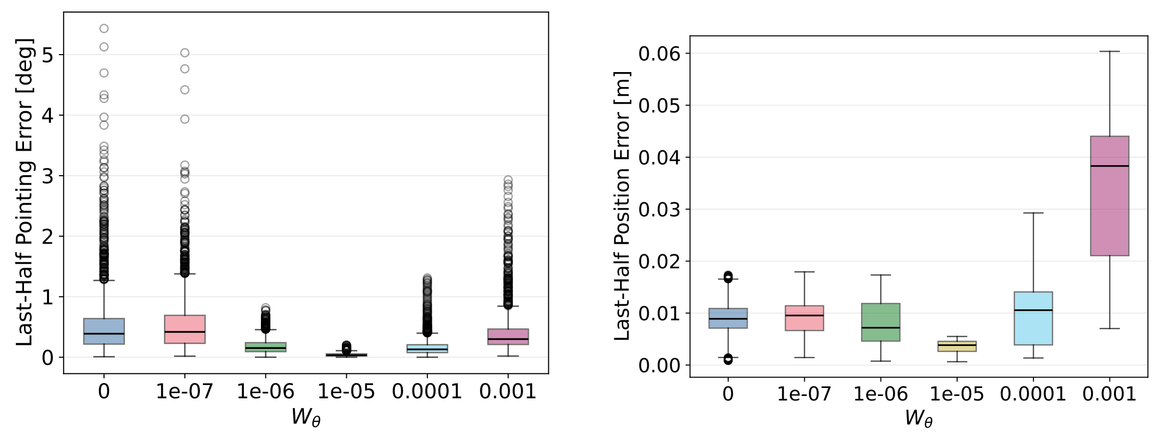

(a) Pointing error

(b) Position error

Figure 12: Closed-loop performance over final half of simulation by joint motion penalty

The commanded joint reconfigurations and corresponding thruster impulse are shown in Figs. 13 and 14. As expected, increasing W_θ decreases the average commanded joint-angle change. The reduction is especially pronounced between $W_\theta = 10^{-6}$ and $W_\theta = 10^{-5}$, after which the optimizer selects much smaller average joint changes for the cases shown. This confirms that the added cost term is effectively biasing the allocation toward nearby arm configurations. However, the reduced joint motion also changes how the commanded wrench is produced. The total commanded impulse initially decreases, consistent with the reduced closed-loop error, and reaches a minimum near $W_\theta = 10^{-5}$. For larger penalty weights, the commanded impulse increases sharply. This increase indicates that once the joint-motion penalty becomes too large, the optimizer relies more heavily on thruster effort because the available configuration changes are overly restricted.

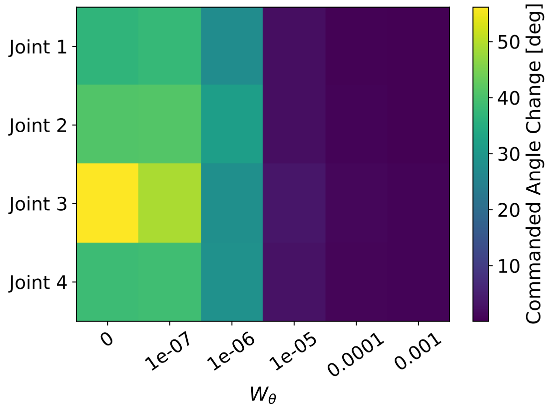

Figure 13: Average commanded joint angle changes for arm 1 by joint motion penalty

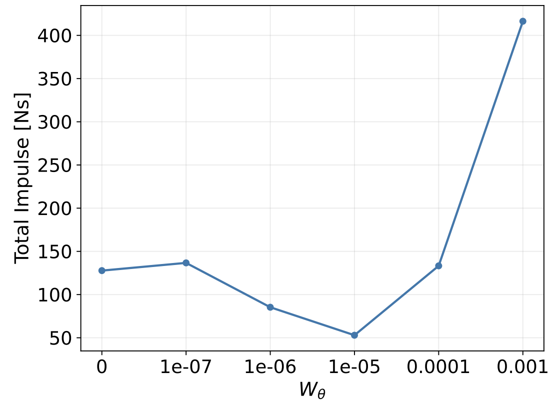

Figure 14: Commanded thruster impulse by joint motion penalty

The reduction in commanded joint motion also improves the joint-settling behavior, as shown in Fig. 15. As W_θ increases, the median settling time decreases and the percentage of unsettled control windows is reduced. For $W_\theta \geq 10^{-5}$, all commanded joint motions settle within the outer-loop control window for the cases considered. This improvement differs from the motion-profile results in the prior section. Rather than increasing the time allowed to execute a given reconfiguration, the motion-aware allocation reduces the size of the commanded reconfiguration itself, making it easier for the joints to settle within the fixed outer-loop control window.

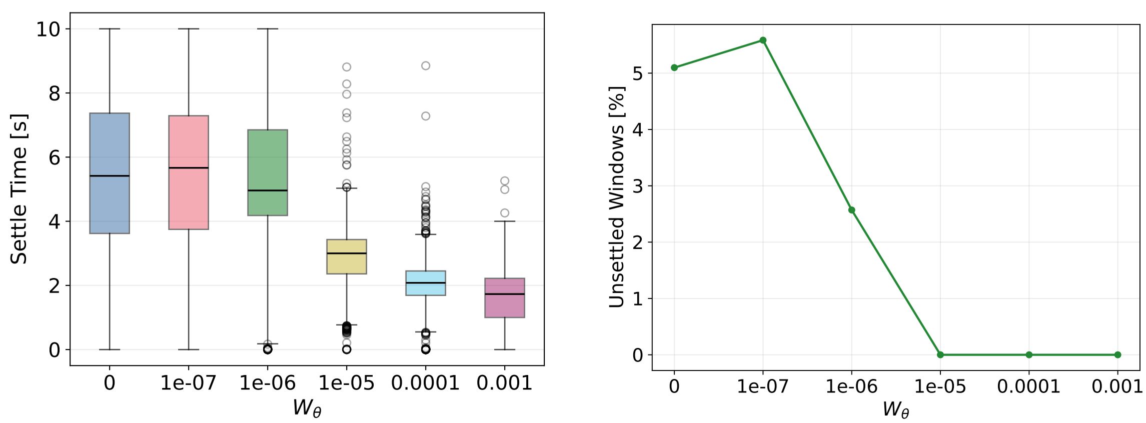

(a) Joint settling times

(b) Control windows where joints do not settle

Figure 15: Joint settling performance by joint motion penalty

These results show that penalizing joint motion in the allocation problem can reduce prescribed hub-torque demand while also improving joint-settling behavior and closed-loop performance. However, these benefits are strongly weight-dependent. If W_θ is too small, the allocation remains close to the baseline solution and little change is observed. If W_θ is too large, the optimizer becomes overly constrained to the current joint configuration, which increases commanded thruster impulse and degrades closed-loop performance. For the simulation considered here, the intermediate value $W_\theta = 10^{-5}$ provides the most favorable balance among prescribed hub-torque reduction, joint-settling reliability, commanded impulse, and position and attitude control performance.

Sensitivity to Manipulator Redundancy

The previous results show that adding a joint-motion penalty to the allocation objective can reduce prescribed hub-torque demand by discouraging unnecessary joint reconfiguration. Because this approach relies on the availability of alternate joint configurations, its effectiveness may depend on the amount of manipulator redundancy available to the allocator. This motivates a sensitivity study in which the number of joints in each arm is varied while applying the same allocation framework.

Increasing the number of joints has two competing effects. Additional joints introduce more actuated coordinates and moving bodies whose accelerations and velocities can contribute to manipulator-induced reaction torques. However, they also expand the configuration space available to the allocation problem. When joint motion is penalized, this added redundancy may allow the optimizer to select nearby configurations that achieve comparable control wrenches with smaller reconfigurations. Therefore, the following results evaluate how additional manipulator redundancy affects the behavior of the joint-motion-aware allocation method.

For the results presented below, the number of joints in each robotic arm is varied while the remaining spacecraft, controller, and mission parameters are kept consistent with the baseline simulation. The 3-DOF arm case is generated by removing the fourth joint from each baseline arm. For the 5-DOF and 6-DOF arm configurations, the original 1 m, 8 kg boom is divided into two 0.5 m, 4 kg sections to provide an additional joint location. The fifth joint rotates about its local 1-axis, while the sixth joint, when included, rotates about its local 2-axis. Each joint-count case is evaluated using both the baseline allocation objective and the joint-motion-aware allocation objective introduced in this section.

Figures 16 and 17 show that increasing the number of joints per arm does not produce a monotonic change in prescribed hub-torque demand. Figure 16 summarizes the typical torque distributions with outliers removed, while Fig. 17 shows the corresponding maximum torque excursions. In the unpenalized case, the additional joint degrees of freedom can be used in dynamically unfavorable ways, leading to larger typical torque distributions and larger peak torque excursions for some higher-DOF cases. This behavior is most evident for the 6-DOF arm, which produces the largest distribution spread in Fig. 16a and the largest maximum prescribed torques in Fig. 17a.

Including the joint-motion penalty substantially reduces the prescribed torque distributions for all joint counts, as shown in Fig. 16b. However, the penalized results remain axis-dependent and non-monotonic with joint count. For example, the 3-DOF case produces the smallest spread about $\hat{b}_2$ and $\hat{b}_3$, while the 6-DOF case produces the smallest spread about $\hat{b}_1$ but a larger spread about $\hat{b}_2$. The 4-DOF and 5-DOF cases remain comparable across the three axes. These results indicate that additional manipulator redundancy is not sufficient by itself to reduce prescribed hub-torque demand.

The maximum prescribed torques in Fig. 17 show that the joint-motion penalty also reduces peak torque excursions. Without the penalty, the 6-DOF arm produces the largest maximum torques, indicating that the added degrees of freedom can be selected in dynamically unfavorable ways when joint motion is not penalized. With the penalty included, the maximum prescribed torques are reduced substantially for all joint counts, and the large peak excursions observed in the unpenalized 6-DOF case are no longer present. The penalized maxima remain axis-dependent and non-monotonic with joint count, but they stay within a much smaller range than in the unpenalized allocation. Thus, the joint-motion penalty mitigates both the typical and peak torque increases that can result from added manipulator redundancy, although it does not make additional joints uniformly beneficial.

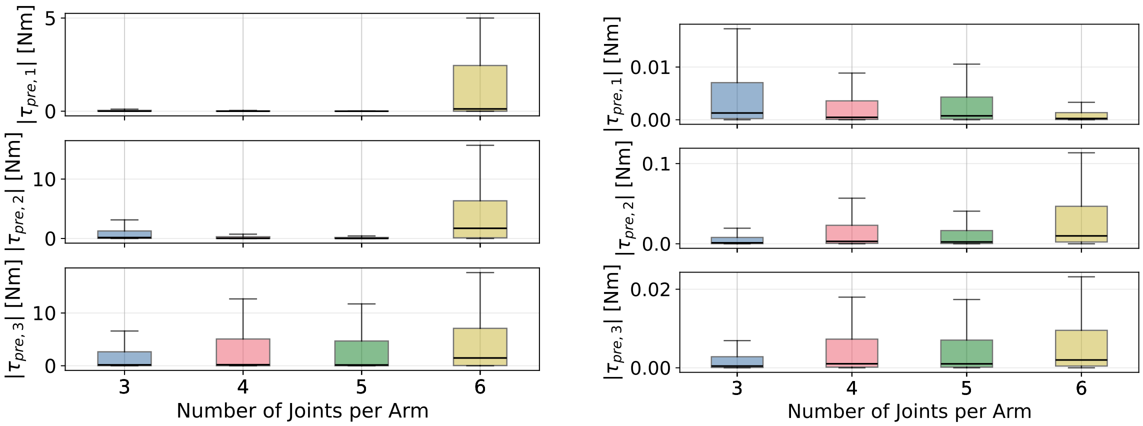

(a) Without joint-motion penalty

(b) With joint-motion penalty

Figure 16: Prescribed hub torque distributions by number of joints per arm with outliers removed

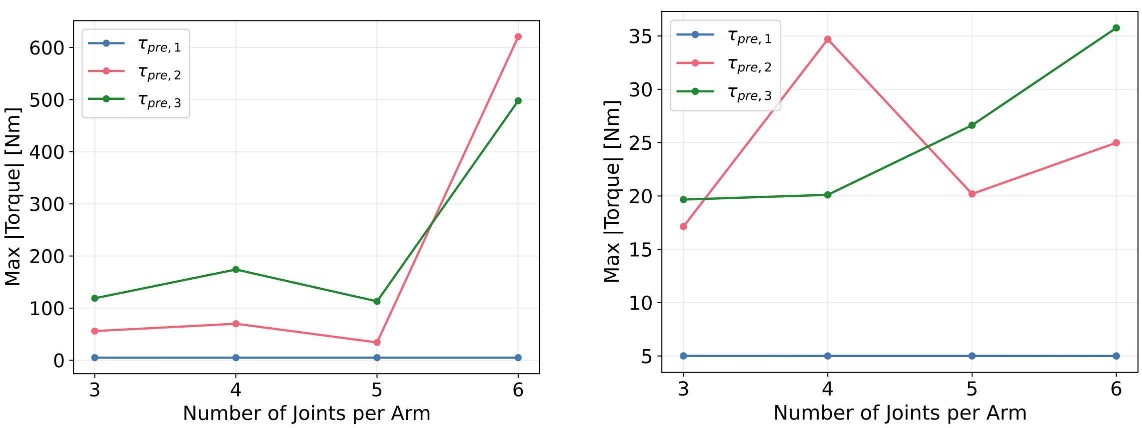

(a) Without joint-motion penalty

(b) With joint-motion penalty

Figure 17: Maximum prescribed hub torques by number of joints per arm

Overall, these results show that the joint-motion-aware allocation method provides a mechanism for reducing prescribed hub-torque demand by discouraging unnecessary joint reconfiguration. The manipulator-redundancy study further shows that this benefit is not obtained simply by increasing the number of joints in each arm. Additional joints expand the available configuration space, but they also introduce additional moving coordinates that can be used in dynamically unfavorable ways if the allocation objective does not appropriately shape the selected motion. With the joint-motion penalty included, both the typical prescribed torque distributions and the maximum torque excursions are substantially reduced across the joint-count cases. Thus, the primary result of this section is that joint motion-reducing allocation design, rather than joint count alone, is the key factor in reducing prescribed hub-torque demand through configuration selection.

CONCLUSIONS

This paper evaluated two approaches for reducing the control torque required to counter manipulator-induced hub reaction torques during rapid arm reconfiguration in a six-degree-of-freedom spacecraft control architecture that uses arm-mounted thrusters for proximity operations. The first approach replaced the baseline joint-regulation controller with a tracking controller that follows finite-duration joint-motion profiles. This change reduced the maximum torque required to counter hub reaction torques by up to 98% and substantially improved pointing performance. The second approach modified the joint-and-thruster allocation problem to penalize large joint motions between consecutive outer-loop updates. This joint-motion-aware allocation reduced the maximum torque required to counter hub reaction torques by up to 88% while also improving closed-loop control performance. The sensitivity of this allocation-based approach to manipulator redundancy was then evaluated by varying the number of joints in each arm. Together, these results show that the reaction-torque burden associated with rapid arm reconfiguration is strongly influenced by both the commanded joint-motion design and the allocation strategy used to select arm configurations.

Future work will expand the configuration studies presented in this paper to evaluate the effects of design choices such as joint arrangement, arm mounting location, and manipulator geometry. In addition, minimum-impulse-bit constraints will be incorporated into the joint-and-thruster allocation problem to address thrust-roundoff effects that contributed to increased position error in the motion-profile cases. These refinements will support the practical implementation of arm-mounted-thruster control for future ISAM proximity-operations missions.

Disclaimer

The views expressed in this article are those of the author and do not reflect the official policy or position of the United States Space Force, Department of Defense, or the U.S. Government.

REFERENCES

[1] D. D. Arney, J. Mulvaney, C. Williams, W. Ruperto-Hernández, J. Friz, C. Stockdale, J. Nelson, and R. Rivera-Vargas, "In-Space Servicing, Assembly, and Manufacturing (ISAM) State of Play," 2024.

[2] J. Lawless, S. Patane, R. Rollins, M. Ledbetter, and R. Cook, "Future ISAM Architectures for National Security Space," *ASCEND 2022*, Las Vegas, Nevada & Online, American Institute of Aeronautics and Astronautics, Oct. 2022, 10.2514/6.2022-4299.

[3] J. N. Opiela, "Orbital Debris Charts, April 2024," Apr. 2024.

[4] P. Th. L. M. van Woerkom and A. K. Misra, "Robotic Manipulators in Space: A Dynamics and Control Perspective," *Acta Astronautica*, Vol. 38, Feb. 1996, pp. 411–421, 10.1016/0094-5765(96)00018-5.

[5] S. A. A. Moosavian and E. Papadopoulos, "Free-Flying Robots in Space: An Overview of Dynamics Modeling, Planning and Control," *Robotica*, Vol. 25, Sept. 2007, pp. 537–547, 10.1017/S0263574707003438.

[6] P. Efimova and D. Shymanchuk, "Dynamic Model of Space Robot Manipulator," *Applied Mathematical Sciences*, Vol. 9, 2015, pp. 4653–4659, 10.12988/ams.2015.56429.

[7] M. Oda, "Coordinated Control of Spacecraft Attitude and Its Manipulator," *Proceedings of IEEE International Conference on Robotics and Automation*, Vol. 1, Apr. 1996, pp. 732–738 vol.1, 10.1109/ROBOT.1996.503861.

[8] L. Shi, J. Katupitiya, and N. Kinkaid, "A Robust Attitude Controller for a Spacecraft Equipped with a Robotic Manipulator," *2016 American Control Conference (ACC)*, July 2016, pp. 4966–4971, 10.1109/ACC.2016.7526140.

[9] I. M. Da Fonseca, L. C. S. Goes, N. Seito, M. K. da Silva Duarte, and É. J. de Oliveira, "Attitude Dynamics and Control of a Spacecraft like a Robotic Manipulator When Implementing On-Orbit Servicing," *Acta Astronautica*, Vol. 137, Aug. 2017, pp. 490–497, 10.1016/j.actaastro.2016.12.020.

[10] A. Antonello, A. Valverde, and P. Tsiotras, "Dynamics and Control of Spacecraft Manipulators with Thrusters and Momentum Exchange Devices," *Journal of Guidance, Control, and Dynamics*, Vol. 42, No. 1, 2019, pp. 15–29, 10.2514/1.G003601.

[11] D. Zlotnik, S. Di Cairano, and A. Weiss, "MPC for Coupled Station Keeping, Attitude Control, and Momentum Management of GEO Satellites Using on-off Electric Propulsion," *2017 IEEE Conference on Control Technology and Applications (CCTA)*, Aug. 2017, pp. 1835–1840, 10.1109/CCTA.2017.8062723.

[12] R. J. Caverly, S. Di Cairano, and A. Weiss, "Split-Horizon MPC for Coupled Station Keeping, Attitude Control, and Momentum Management of GEO Satellites Using Electric Propulsion," *2018 Annual American Control Conference (ACC)*, June 2018, pp. 652–657, 10.23919/ACC.2018.8431329.

[13] R. J. Caverly, S. Di Cairano, and A. Weiss, "On-Off Quantization of an MPC Policy for Coupled Station Keeping, Attitude Control, and Momentum Management of GEO Satellites," *2018 European Control Conference (ECC)*, June 2018, pp. 1–6, 10.23919/ECC.2018.8550336.

[14] R. Caverly, S. Di Cairano, and A. Weiss, "Control Allocation and Quantization of a GEO Satellite with 4DOF Gimbaled Thruster Booms," *AIAA Scitech 2020 Forum*, Orlando, FL, American Institute of Aeronautics and Astronautics, Jan. 2020, 10.2514/6.2020-1687.

[15] Z. Wei, T. Long, R. Shi, and X. Song, "Electric Thruster Configuration Design Optimization for Geostationary Satellites with Robotic Manipulators," *Advances in Space Research*, Vol. 69, May 2022, pp. 3798–3813, 10.1016/j.asr.2022.02.048.

[16] A. Prakash and D. K. Giri, "Design and Dynamical Analysis of a Novel 6-DOF Spacecraft Maneuvering System Using Robotic Manipulator-Based Thruster System," *AIAA SCITECH 2025 Forum*, Orlando, FL, American Institute of Aeronautics and Astronautics, Jan. 2025, 10.2514/6.2025-0408.

[17] W. Schwend and H. Schaub, "Cascaded Control Architecture for Spacecraft with Arm-Mounted Thrusters using Reaction Torque Compensation," *Journal of Spacecraft and Rockets*, 2026. In review.

[18] F. Sena, R. Vijayan, H. Mishra, and M. D. Stefano, "Center-of-Mass and Attitude Control of an Orbital Manipulator: A Novel Control Strategy," *IEEE Robotics and Automation Letters*, Vol. 11, June 2026, pp. 6871–6878, 10.1109/LRA.2026.3682621.

[19] W. Schwend and H. Schaub, "Planar Spacecraft Control Through One Degree of Freedom Time-varying Thruster Configurations," *AAS/AIAA Astrodynamics Specialist Conference*, Aug. 2025.

[20] R. Featherstone, *Rigid Body Dynamics Algorithms*. Boston, MA: Springer, 2008, 10.1007/978-1-4899-7560-7.

[21] E. Todorov, T. Erez, and Y. Tassa, "MuJoCo: A Physics Engine for Model-Based Control," *2012 IEEE/RSJ International Conference on Intelligent Robots and Systems*, Oct. 2012, pp. 5026–5033, 10.1109/IROS.2012.6386109.

[22] J. Garcia Bonilla and H. Schaub, "A Message-Passing Simulation Framework For Generally Articulated Spacecraft Dynamics," *AAS/AIAA Astrodynamics Specialist Conference*, Boston, MA, August 10–14 2025. Paper No. AAS 25-801.

[23] J. Garcia Bonilla, W. Schwend, and H. Schaub, "Simulation of Generally Articulated Spacecraft for GNC Algorithm Design and Validation," *AAS Guidance, Navigation and Control Conference*, Breckenridge, CO, Jan. 31 – Feb. 4 2026. Paper No. AAS 26-078.

[24] H. Schaub and J. L. Junkins, *Analytical Mechanics of Space Systems*. Reston, VA: AIAA Education Series, 4th ed., 2018, 10.2514/4.105210.

[25] R. Mukherjee and D. Chen, "Asymptotic Stability Theorem for Autonomous Systems," *Journal of Guidance, Control, and Dynamics*, Vol. 16, Sept. 1993, pp. 961–963, 10.2514/3.21108.

[26] K. M. Lynch and F. C. Park, *Modern Robotics: Mechanics, Planning, and Control*. Cambridge University Press, 1 ed., May 2017, 10.1017/9781316661239.